Journal of Materials Chemistry B

Accepted Manuscript

ROYAL SOCIETY OF CHEMISTRY

www.rsc.org/materialsB

Mesoporous Nanoparticles Gd_2O_3@mSiO_2/$ZnGa_2O_4$: Cr^{3+}, Bi^{3+} as a Multimodal Probe for Magnetic Resonance Imaging, Drug Delivery and Targeted Bioimaging

W. B. Dai, [a, ♥] Y. F. Lei, [b, ♥] S. Ye, [a] E. H. Song, [a] Z. Chen [a] and Q. Y. Zhang [♣, a]

[a] *State Key Laboratory of Luminescent Materials and Devices, South China University of Technology, Guangzhou, 510640, China*
[b] *Laboratory for Biological Effects of Nanomaterials and Nanosafety, National Center for Nanoscience and Technology, Beijing, 100190, China*

.

Abstract: Red/near infrared (NIR) persistent luminescence nanoparticles (PLNPs) hold great potential as a new generation of probes for detection and imaging of biomolecules. Based upon the consideration that a single nanoprobe could serve multiple purposes, the development of multimodal nanoprobe that combined properties of rechargeable persistent emitting luminescence, magnetic resonance imaging (MRI) and drug delivery has arisen our attention as promsing prospect in the filed of nanotechnologies directed toward biomedical applications. Herein, mesoporous nanoparticles Gd_2O_3@mSiO_2/$ZnGa_2O_4$: Cr^{3+}, Bi^{3+} (ZGOCB) that exhibit enhancement of red (~ 695 nm) persistent luminescence (~ 18 d) property were synthesized by using mesoporous silica nanospheres both as morphology-controlling templates and vessels. Being composed of hybrid shell/core architecture and through surface functionalization, the mesoporous nanoparticles Gd_2O_3@mSiO_2/ZGOCB possess capacity for *in vivo* and *in situ* real-time monitoring, targeting tumors and drug delivery. Simultaneously, Gd_2O_3@mSiO_2/ZGOCB exhibits a prominent longitudinal relaxivity, indicating these nanoparticles could be also used as magnetic resonance imaging agents. We believe that this rechargeable red persistent luminescence and MRI-based core/shell structure of multimodal nanoprobe offers a promising nano-platform for both diagnostics and therapeutics of reactive species in living cells or *in vivo*.

Keywords: Renewable long afterglow; Real-time monitoring; Drug delivery; Magnetic resonance imaging; Mesoporous nanoprobes

♣ Corresponding author, E-mail: qyzhang@scut.edu.cn
♥ W. B. Dai and Y. F. Lei contributed equally to this work.

1. Introduction

Nanotechnology-based nanomaterials have been demonstrated to be very useful in the medical diagnosis, therapy of various diseases and basic biological research. [1] Persistent luminescent nanoprobes (PLNPs) can be stimulated to release their storage energy based on thermal luminescence (can occur at room temperature (RT) if the energy provided is sufficient to activate the release of carriers) or by using light of an appropriate energy. [2] The temporal separation of excitation and afterglow makes PLNPs ideal as optical imaging contrast agents. Especially, red or near-infrared (NIR) PLNPs have been expected to be used for *in vivo* optical imaging tools owing to the advantages of high biopenetration (in the range of "biological window", where the lowest absorption coefficient of tissue can be observed) and high signal-to-noise ratio (SNR, avoid the interference of autofluorescence (λ < 600 nm) from the elastin, collagen and other biological fluorophores, resulting in background-free condition). [3]

In view of their remarkable red/near infrared (NIR) long-lasting emitting nature, there has been increasing interest in adopting PLNPs as *in vivo* bioimaging agents. Scherman et al. reported a pioneering work to realize *in vivo* bioimaging for more than 1 h by using persistent PLNPs $Ca_{0.2}Zn_{0.9}Mg_{0.9}Si_2O_6$: Eu^{2+}, Mn^{2+}, Dy^{3+}. [3a] After that, serveral NIR emitting PLNPs such as $Zn_3Ga_2Ge_2O_{10}$: Cr^{3+}, $CaMgSi_2O_6$: Eu^{2+}, Mn^{2+}, Pr^{3+}, $Zn_{2.94}Ga_{1.96}Ge_2O_{10}$: Cr^{3+}, Pr^{3+} and $LiGa_5O_8$: Cr^{3+} have been reported for *in vivo* bioimaging in small animals without background noise. [3c, 4] Although the PLNPs surmount the autofluorescence from living tissues and enable highly sensitive detection, the persistent luminescence can not be effectively activated *in situ*, impeding their long-term observations in living animals. Till recently, this critical shortcoming was overcome by discovery of a series of novel nanoparticles such as $ZnGa_2O_4$: Cr^{3+} (ZGOC), whose persistent luminescence can be repeatedly activated through living tissues under a simple orange-red LED source. [5] However, from another point of view, although the above mentioned rechargeable PLNPs hold great promising for long-term bioimaging with high SNR, they still are beyond their grasp as drug carriers due to the lacking of porous structure and uniform particles. Typically, mesoporous silica ($mSiO_2$) can be used as promising drug carriers because of stable mesoporous structure, high specific surface area and good biocompatibility. [6] Alone using $mSiO_2$ as drug carriers is impossible to monitor in real-time or

effectively locate targeted site (i.e., tumor) due to the lack of detectable signals. Considerable attention has been paid on combining $mSiO_2$ with recognizable PLNPs form trackable drug carriers such as $mSiO_2$/ZGOC, which introduced a nano-platform based on persistent luminescence for both *in vivo* optical imaging and drug delivery. [5, 6d] Magnetic resonance imaging (MRI) is another noninvasive diagnostic tool which can offer opaque tissue contrast and good spatial resolution. The shortcoming of MRI is its low sensitivity. [6c, 7] Based upon the ambitious idea that one single nanoparticle serves simultaneously multiple purposes, the combination use of MRI and optical imaging techniques can bridge the gap in resolution, sensitivity and the depth of living tissues imaging directed toward biological imaging applications. As far as we know, nanoprobe coinstantaneously possesses the properties of rechargeable long persistent luminescence and magnetism integrated drug carriers has not been reported yet.

On a single doped ion, Cr^{3+} is ideal candidate for obtaining red or NIR persistent luminescence since its $3d^3$ electron configuration allows a narrow-band emission (ca. ~ 695 nm) due to the spin-forbidden $^2E \rightarrow {}^4A_2$ transition or a broadband emission (ca. 650 ~ 1600 nm) ascribed to the spin-allowed $^4T_2 \rightarrow {}^4A_2$ transition. [3a, 3b, 4b, 4c, 5] Bulky size of red persistent luminescence of ZGOC was reported by Bessière in 2011. [8] Under ideal condition, the ZGO composes of tetrahedrally coordinated Zn^{2+} and octahedrally coordinated Ga^{3+}. Real ZGO contains some degree of antisite coordination. The antisites are the key internal defects responsible for Cr^{3+} persistent luminescence with slightly Zn-deficient. [3c, 9] Typically, for further improving persistent luminescence properties, finding an appropriate codopant not only benefits optical properties but also contributes to revealing important information on mechanism. In this contribution, we report the improvement of red PLNPs $Zn_{0.97}G_2O_{3.97}$: $0.01Cr^{3+}$, $0.02Bi^{3+}$ (ZGOCB) by a biphasic synthesis route. Meanwhile, the $mSiO_2$ is employed as drug carriers and morphology-controlling templates to design the core/shell structure nanoprobe Gd_2O_3@$mSiO_2$/ZGOCB. Taking advantage of the properties of biocompatibility, rechargeable red persistent luminescence, narrow size distribution and large pore capacity, the Gd_2O_3@$mSiO_2$/ZGOCB is suitable for both highly sensitive optical detection *via* living tissues and concomitant drug delivery. Meanwhile, due to the presence of Gd_2O_3, the Gd_2O_3@$mSiO_2$/ZGOCB possesses the property of magnetism and indicates it can be simultaneously used as MRI agent.

Moreover, through surface functionalizaiton with a tumor-targeting group folic acid (FA), the Gd_2O_3@$mSiO_2$/ZGOCB shows tumor-targeting ability both *in vitro* and *in vivo* with high SNR. Employing doxorubicin (Dox) as a drug model, we also demonstrates this nanoprobe can be successfully loaded with anticancer agent and subsequently initiate its progressive release *in situ* to cure tumors. Altogether, the prepared Gd_2O_3@$mSiO_2$/ZGOCB multimodal nanoprobe offers simultaneously great potential for drug delivery, MRI and optical bioimaging.

2. Results and discussion

Formation, morphology and porous structure. The design of preparing involved formation of $mSiO_2$ as morphology templates and following by synthesis of Gd_2O_3 and ZGOCB nanoclusters inserting into its pores. Along with evolution of nanoparticle size, the encapsulation of Gd_2O_3 and ZGOCB in $mSiO_2$ goes with a substantial change in surface properties. Transmission electron microscopy (TEM) image clearly shows ZGOCB NPs are nearly monodisperse (Figure S1a, S: supporting information, hereinafter) with ~ 8 nm size (7.6 nm ± 1.1 nm, value obtained from 300 randomly selected particles, Figure S1b). High-resolution TEM analysis indicates these NPs are single crystalline and nearly spherical. The distance between the lattice fringes for the *d*-spacing of the (111) plane is ~ 4.79 Å, which is agreement with the spinel ZGO (Figure S1c). The electron diffraction pattern of a typical selected area of ZGOCB shows rings from the (220), (311), (400), (422), (511), (440) and (533) planes of the cubic ZGO (Figure S1d).

Meanwhile, TEM image shows the carriers $mSiO_2$ possesses regular spherical morphology and narrow size distribution (~ 60 nm, inset of **Figure 1**a). XRD low angle diffraction pattern confirms the mesoporous silica structure (Figure 1a). The SEM and TEM images (Figures 1b and 1c) reveal that Gd_2O_3@$mSiO_2$/ZGOCB has the monodisperse spherical morphology (with the average diameter ~ 200 nm) and core/shell structure. The dark color spheres are assigned to the Gd_2O_3 spherical core and the light color external thin places belong to the silica shell and ZGOCB, respectively (Figure 1c). The XRD patterns (Figure 1d) show the Gd_2O_3@$mSiO_2$/ZGOCB is matching well with the phases of cubic ZGO (JCPDS file No.: 38-1240) and Gd_2O_3 (JCPDS file No.: 43-1014), indicating presence of mixture of Gd_2O_3 and ZGOCB in $mSiO_2$. The EDS results (Figure 1e) further reveal the co-existence of

elements including Zn, Gd, Si, Cr and Bi. These results suggest the core/shell architecture of the Gd_2O_3@$mSiO_2$/ZGOCB is successful obtained.

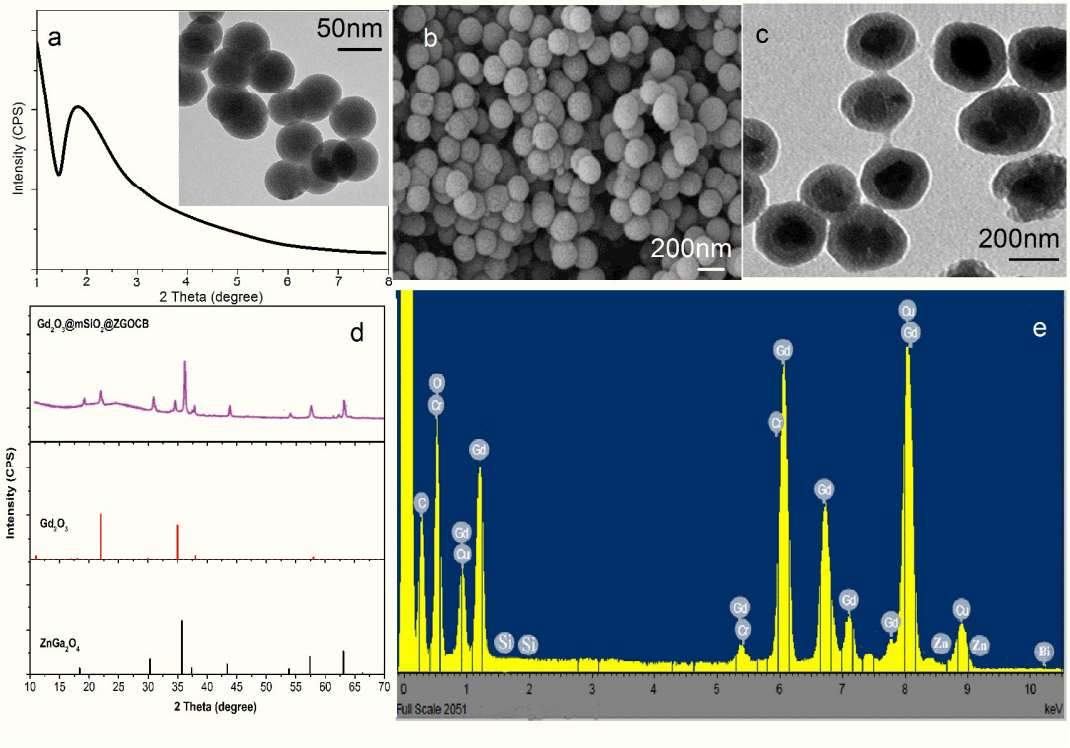

Figure 1. (a) XRD low angle diffraction pattern and inset shows TEM image of $mSiO_2$. (b-e) FESEM, TEM, XRD patterns and EDS pattern of the Gd_2O_3@$mSiO_2$/ZGOCB, respectively.

Since formation of mesoporous framework of the nanoprobe is essential in this study, N_2 adsorption/desorption was employed to examine the specific surface area and pore size distribution of the $mSiO_2$ and Gd_2O_3@$mSiO_2$/ZGOCB. Mesoporous characteristics of plateau regions (typical type-IV isotherms) are formed both for the $mSiO_2$ and Gd_2O_3@$mSiO_2$/ZGOCB (**Figure 2**a). According to the Brunauer-Emmett-Teller (BET) method, [10] the specific surface area of the $mSiO_2$ and Gd_2O_3@$mSiO_2$/ZGOCB are calculated to be ~ 537.4 and 203.6 $m^2 \cdot g^{-1}$ with the pore volumes are ~ 0.3352 and 0.1536 $cm^3 \cdot g^{-1}$, respectively, due to the formation of Gd_2O_3 and ZGOCB in the pores of the $mSiO_2$ structure. The formation of core/shell structure Gd_2O_3@$mSiO_2$/ZGOCB based on the $mSiO_2$ templates decreases the average pore volume of the carriers (a slight decrease in average pore size from 3.016 to 2.214 nm was calculated, Figure 2b), which can be explained by the fact that the

Gd_2O_3 and ZGOCB are isolated in the channels within the $mSiO_2$. Actually, the combination of this uniform mesoporous core/shell structure is highly favorable for drug delivery application.

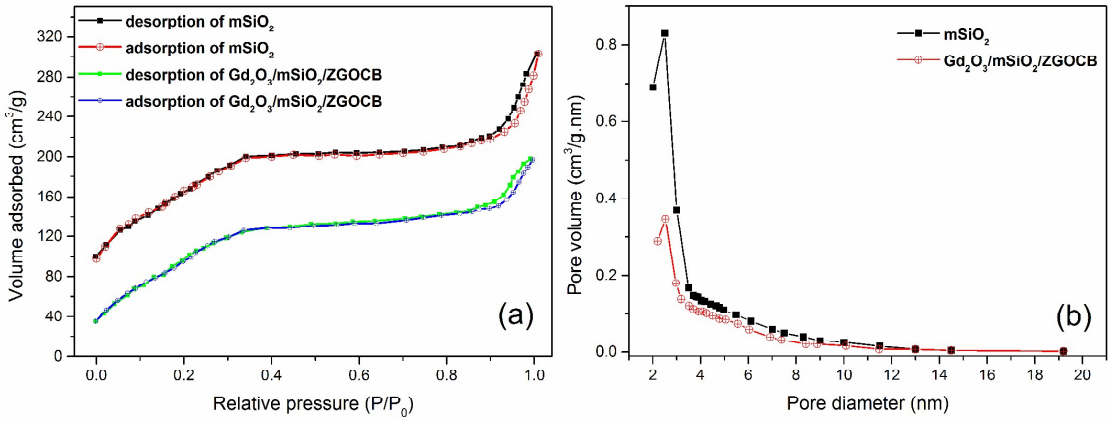

Figure 2. (a) N_2 adsorption/desorption isotherms and (b) pore size distributions of $mSiO_2$ and Gd_2O_3@$mSiO_2$/ZGOCB NPs.

Surface functionalization and cytotoxicity assay. For improving the colloidal stability, biocompatibility and tumor targeting ability, FA was needed to graft onto the surface of Gd_2O_3@$mSiO_2$/ZGOCB. The three-step procedure of modification as well as the application of the multimodal nanoprobe Gd_2O_3@$mSiO_2$/ZGOCB is shown in **Scheme 1**. Firstly, the Gd_2O_3@$mSiO_2$/ZGOCB was treated with NaOH to create OH^- groups on the surface. Then, APTES reacted with surface hydroxyl groups to make amine functionalization and form Gd_2O_3@$mSiO_2$/ZGOCB-NH_2. Finally, FA was grafted onto the amino group for tumor targeting. The FT-IR and zeta potential measurements during different surface modification process were employed to monitor the change of surface functional group. As shown in **Figure 3**a, an absorption band at ~ 3400 cm^{-1} (O-H) indicates the OH^- groups were successful grafted. After amination, there are absorption bands at ~ 1130 and 1050 cm^{-1} (stretching vibration of O-Si-O), the asymmetric and symmetric CH_2- stretching bands at ~ 2920 and 2860 cm^{-1} and the N-H stretching bands at ~ 3400 and 3300 cm^{-1} indicate the successful modification Gd_2O_3@$mSiO_2$/ZGOCB with APTES. The absorption bands located at ~ 1500 cm^{-1} (amide II band) and ~ 1640 cm^{-1} (stretching vibration of C=O) indicates the FA was grafted onto the surface of Gd_2O_3@$mSiO_2$/ZGOCB. [3c, 4c, 11]

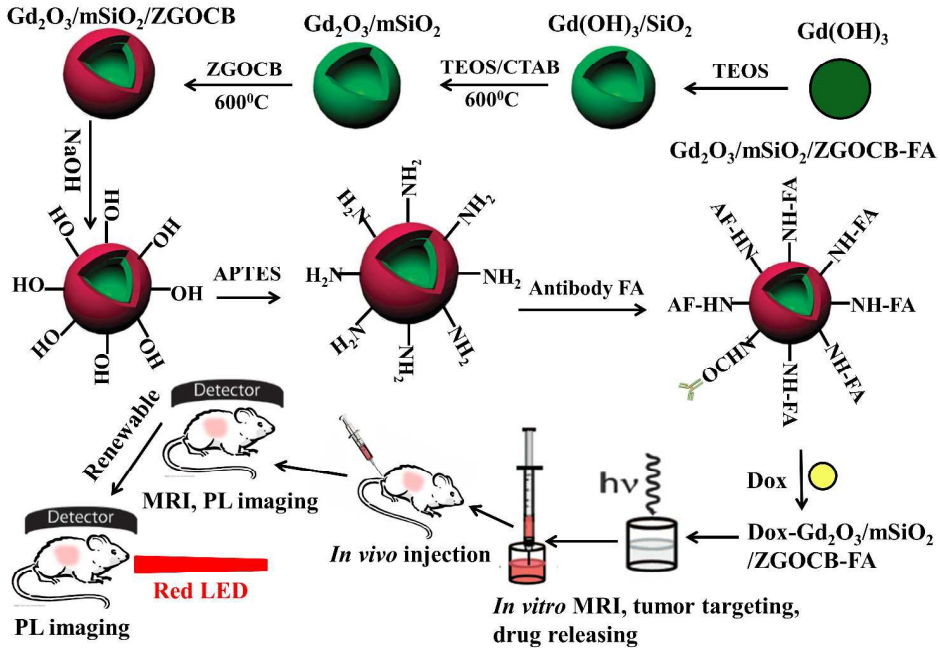

Scheme 1. Schematic illustration of the synthesis, surface functionalization and application of the core/shell structure nanoprobe Gd_2O_3@$mSiO_2$/ZGOCB.

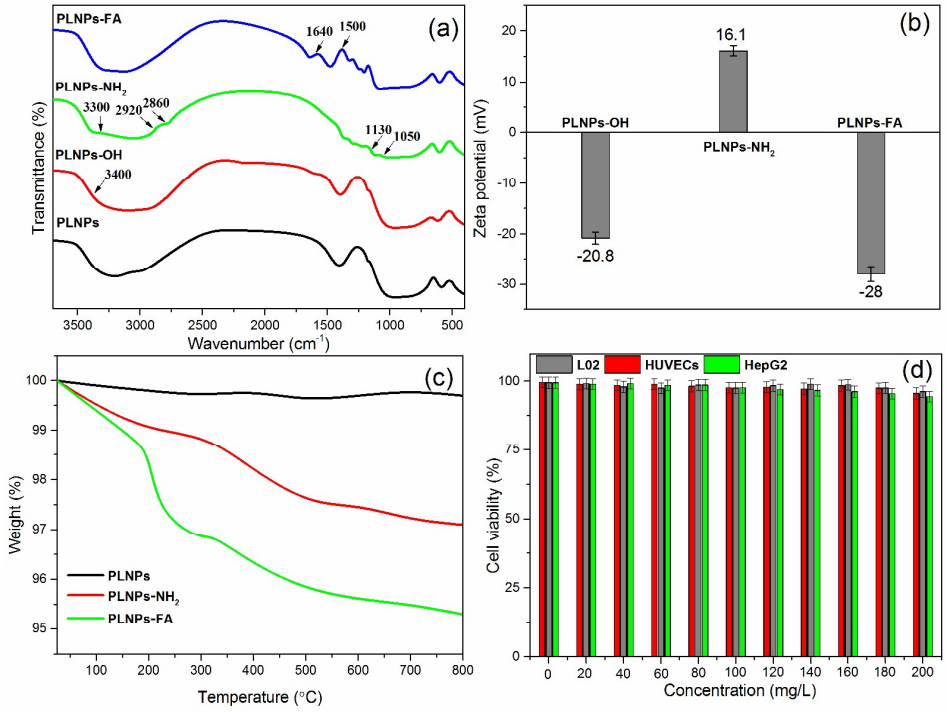

Figure 3. (a-c) FT-IR spectra, zeta potentials and TGA curves of surface modified nanoprobe Gd_2O_3@$mSiO_2$/ZGOCB, respectively. (d) MTT cell viability assay.

On the other hand, the change of zeta potential can also prove the success of modification (Figure 3b). After reaction with NaOH, zeta potential became negative (-20.8 mV) which proves OH^- groups were modified on the surface. The sample further treated with APTES gave the positive surface potential (+16.1 mV). Finally, the zeta potential switched again from positive to negative value (-28 mV), which confirms the formation of the tumor targeting Gd_2O_3@$mSiO_2$/ZGOCB-FA. [4c, 6a, 6c] Furthermore, the amounts of APTES and FA grafted onto the surface of Gd_2O_3@$mSiO_2$/ZGOCB were estimated by thermogravimetric analysis (Figure 3c). Below 150°C, a slight weight loss was observed for both the Gd_2O_3@$mSiO_2$/ZGOCB-NH_2 and Gd_2O_3@$mSiO_2$/ZGOCB-FA due to the loss of absorbed water. At higher temperature, a sharp drop of weight for Gd_2O_3@$mSiO_2$/ZGOCB-FA occurred due to the pyrolysis of FA, which is agreement with the weight loss curve of pure FA (Figure S2). The weight percentages of organic moieties on Gd_2O_3@$mSiO_2$/ZGOCB-NH_2 and Gd_2O_3@$mSiO_2$/ZGOCB-FA were calculated to be ~ 2.9% and 4.7%, respectively.

Low toxicity is critical requirement for *in vivo* studies. [1, 2a, 2c,3a, 3c, 5, 6a, 6c] The cytotoxicity of the Gd_2O_3@$mSiO_2$/ZGOCB-NH_2 was tested on L02, HUVECs and HepG2 cells using the MTT and apoptosis assays. The viabilities of the three type cells were all greater than 90% (94.5%, 95.1% and 93.3% for the L02, HUVECs and HepG2 cells, respectively) after incubation of the cell lines with Gd_2O_3@$mSiO_2$/ZGOCB-NH_2 under the concentration as high as 200 $mg \cdot L^{-1}$ for 24 h (Figure 3d), which indicates low toxicity of Gd_2O_3@$mSiO_2$/ZGOCB-NH_2 to all cells. The apoptosis assay was also confirmed the conclusion (Figure S3a). The percentage of viable cells was 95.7%, 93.6% and 97.1% for L02, HUVECs and HepG2 cells, respectively, when the concentration of Gd_2O_3@$mSiO_2$/ZGOCB-NH_2 reached to 200 $mg \cdot L^{-1}$. Moreover, the long-term toxic effect of Gd_2O_3@$mSiO_2$/ZGOCB-NH_2 was also assessed using mice (Figure S3b). After one month of injection (0.5 mL, 200 $mg \cdot L^{-1}$), the mice viability was still 100% and there was no significant difference between the body weights of control and treated mice. To furhter confirm the low toxicity of the modified nanoprobe, the Dox-Gd_2O_3@$mSiO_2$/ZGOCB-FA was also tested using the MTT cell viability method (Figure S3c). Similar to the Gd_2O_3@$mSiO_2$/ZGOCB-NH_2, the viabilities of the three type cells were also all greater than 90%. The above results indicate the low toxicity of the modified nanoprobe Gd_2O_3@$mSiO_2$/ZGOCB.

Rechargeable long-lasting red luminescence properties. The primary composition was fixed as $Zn_{0.97}Ga_2O_{3.97}$ with 3% Zn deficiency, which could improve the long afterglow properties. [3c, 9] The Cr^{3+} and Bi^{3+} ions prefer to occupy the octahedrally site of Ga^{3+} because of the approximate ionic radii between Ga^{3+} and Cr^{3+}/Bi^{3+} and the strong ligand-field stabilization energy of Cr^{3+} in 6-fold coordination. [3d, 12] However, it cannot be completely ruled out partial Bi^{3+} ions enter into Zn^{2+} sites since the difference between their ionic radii is also small. Hence, with introducing these ions, it would induce distortion in the ZGO crystal and antisite defects should appear to compensate for excessive positive charges. The decay curves of $Zn_{0.97}Ga_{2-x-y}O_{3.97}$: $x$$Cr^{3+}$, $y$$Bi^{3+}$ varied with the contents of Cr^{3+} and Bi^{3+} (Figure S4a). The persistent luminescence intensity decreased as the content of Cr^{3+} increased (no more than 0.01) because the increased Cr^{3+} emitter made a quicker release of the energy of excitation storage and faster decay of persistent emission. The optimal doping rate for these ions is fixed at 1% and 2% for Cr^{3+} and Bi^{3+}, respectively.

Figure 4a shows diffuse reflectance spectra of NPs of ZGO: 0.02Bi, ZGO: 0.01Cr and ZGO: 0.01Cr, 0.02Bi. The absorption bands at < 350, 350-470 and 470-650 nm attributed to the band-to-band transition of ZGO, $^4A_2 \rightarrow {}^4T_1$ and the $^4A_2 \rightarrow {}^4T_2$ transitions of Cr^{3+} are largely enhanced in the ZGO: 0.01Cr, 0.02Bi. Among these bands, the absorbance at the range between 600-650 nm is responsible for *in vivo* recharging by using deeper-tissue-penetrating red light. The absorption band associated to Bi^{3+}: $^1S_0 \rightarrow {}^3P_1$ transition (360 nm) or Bi^{3+}-Bi^{5+} charge transfer state (450 nm), which was observed in stoichiometric ZGO: Bi^{3+} phosphor, [13] cannot be identified in the ZGO: 0.01Cr, 0.02Bi. Figure 4b shows PLE and PL spectra of the ZGO: 0.01Cr and ZGO: 0.01Cr, 0.02Bi. The spectral shapes are almost identical. The emission structure of the N_2 line at 695 nm, the R line at 688 nm and phonon side bands (PBS) are consistent with those reported in the literature. [2a, 3d, 4b, 4c, 6a, 6d] With regard to the relative intensity, the ZGO: 0.01Cr, 0.02Bi shows ~ 2.5 times higher than ZGO: 0.01Cr both for the PL and PLE spectra.

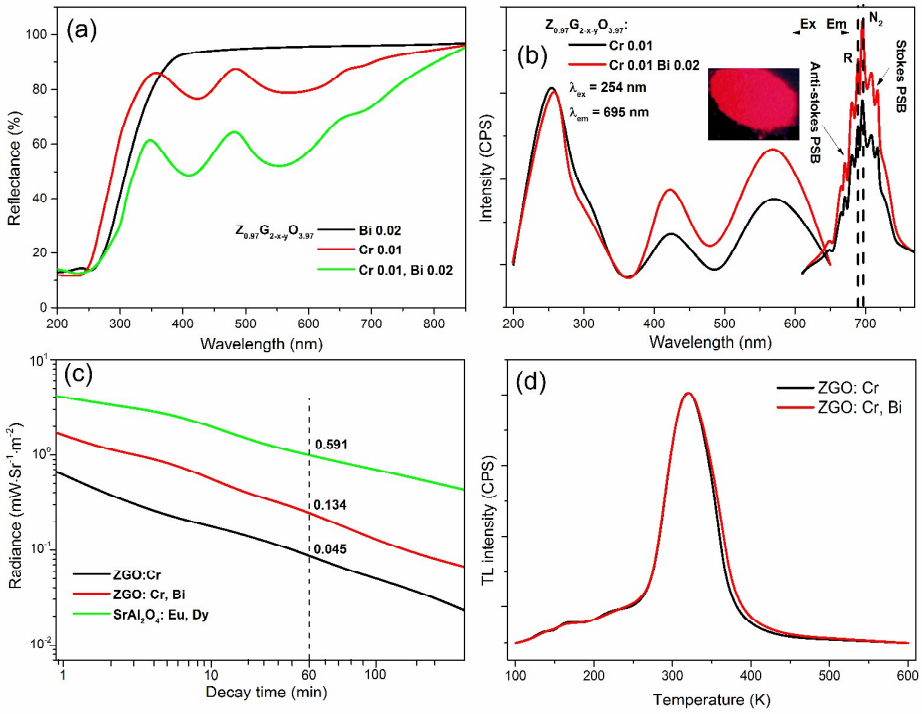

Figure 4. (a) Diffuse reflectance spectra. (b) PLE and PL spectra (77K), the inset is powder digital photo under 254 nm hand-held lamp excitation. (c) Radiance of persistent luminescence at RT. All the samples were excited by UV light from a 300 W xenon lamp for 5 min. (d) TL glow curves.

The afterglow decay curves of the ZGO: 0.01Cr and ZGO: 0.01Cr, 0.02Bi with a reference $SrAl_2O_4$: Eu, Dy [14] are plotted in Figure 4c. Great improvement of persistent luminescence intensity by Bi^{3+} codoping was observed (also see Figure S4a). In one hour after removal of UV excitation, the ZGO: 0.01Cr, 0.02Bi showed radiance of 0.134 $mW \cdot sr^{-1} \cdot m^{-2}$, which is ~ 3 times higher than that of ZGO: 0.01Cr. This value is comparable to the radiance of persistent luminescence of $SrAl_2O_4$: Eu, Dy (0.591 $mW \cdot sr^{-1} \cdot m^{-2}$) since Cr^{3+} emission in ZGO: 0.01Cr, 0.02Bi is not sensitive to human eyes. However, red or NIR emission is highly sensitive to common optoelectronic devices and highly transmissive to biological tissues. The red afterglow could be detected after 18 days without any further illumination, suggesting the ZGOCB has good potential for optical imaging application (Figure S4b).

An unfavorable self-reduction effect would be occurred with stoichiometric variation in the Zn-deficient ZGO as expressed by Equ (1). [12d] For preserving the spinel crystallinity, the excess Ga atoms are partially incorporated into tetrahedral sites and form positive antisite defects $Ga_{Zn}^{\bullet}$. To

maintain the charge balance, an equal amount of free electrons would be produced. These resultant electrons would couple with dopants. This reduction effect can be verified in the Bi-doped $Zn_{0.97}Ga_2O_{3.97}$ compound, where Bi^{3+}-related absorptions at 360 and 450 nm, as observed in stoichiometric compound, were totally absent because of the reduction of Bi^{3+} (Figure 4a) as expressed by the Equ (2).

$$3Ga_2O_3 \xrightarrow{ZGO} 2Ga_{Zn}^{\bullet} + 4Ga_{Ga}^{x} + 8O_O^x + 0.5O_2 \uparrow + 2e' \quad (1)$$

$$Bi^{3+} + 3e' \rightarrow Bi^0 \quad (2)$$

As a result, without Bi^{3+}, a portion of Cr^{3+} would be reduced. Conversely, Bi^{3+} may preferentially accept resultant electrons since Bi^{3+} are easier to reduce than Cr^{3+} in most hosts [15] and Cr^{3+} is avoided from reduction. Therefore, improvements of Cr^{3+} absorption, PL and persistent luminescence are considered consequences of the stabilization of Cr^{3+} ions. Moreover, the comparison of TL curves (Figure 4d) between ZGO: 0.01Cr and ZGO: 0.01Cr, 0.02Bi suggests the defects responsible for Cr^{3+} persistent luminescence are almost unchanged with Bi^{3+} codoping. Namely, the defects are still originated from intrinsic structure within the ZGO matrix (not introduced by Bi^{3+} codoping).

When using ZGOCB, Gd_2O_3 and $mSiO_2$ made up Gd_2O_3@$mSiO_2$/ZGOCB nanoprobe and through functionalization with FA, the Gd_2O_3@$mSiO_2$/ZGOCB-FA was easily dissolved in water to form a luminescence solution. Compared to the powder form of ZGOCB, except the intensity was lower (perhaps due to the quenching effect of the O-H vibration of water [1e]), the PL spectrum of the Gd_2O_3@$mSiO_2$/ZGOCB-FA solution showed similar emission bands under UV excitation (Figure S5a). It is needed to emphasize that the Gd_2O_3@$mSiO_2$/ZGOCB-FA solution still shows long-lasting red luminescence after irradiation with UV light for 2 min. Nevertheless, the afterglow signal can be recovered and persisted for a long time after re-irradiation by red light (Figure S5b), indicating the obtained nanoprobe can be easily utilized in *in vivo and in situ* real-time monitoring.

***In vitro* and *in vivo* MRI.** Typically, Gd^{3+}-containing nanoprobes S5b), indicating the obtained nanoprobe can be easily utilized in *in vivo and in situ* real-time monitoring.show potentials as MRI contrast agent since their positive signal-enhancement ability. [6c, 7] To evaluate the capability of the Gd_2O_3@$mSiO_2$/ZGOCB for MRI application, longitudinal proton relaxation times (T_1) were determined as a function of Gd^{3+} concentration (0 ~ 1 mM, **Figure 5**a). The T_1-weighted images

gradually become brighter, suggests a positive enhancement of the effect on T_1-weighted sequences. Relaxivity measurement show that the Gd_2O_3@$mSiO_2$/ZGOCB has a concentration-dependent proton longitudinal relaxivity (r_1) of ~ 6.68 $mM^{-1}\cdot s^{-1}$ on the 7 T MRI system (Figure 5a), indicating the potential of Gd_2O_3@$mSiO_2$/ZGOCB as effective contrast agent for T_1-weighted MRI.

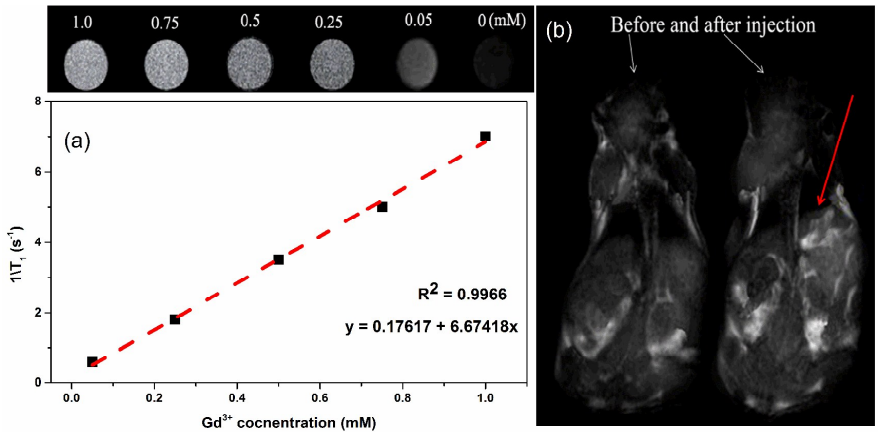

Figure 5. (a) T_1-weighted MR images of Gd_2O_3@$mSiO_2$/ZGOCB. (b) Before and after intravenous injection of Gd_2O_3@$mSiO_2$/ZGOCB-NH_2 (0.15 mg) T_1-weighted MR images of a mouse, the red arrow shows the liver.

For *in vivo* MRI application, T_1-weighted MRI of Kunming mice before and after intravenous injection of Gd_2O_3@$mSiO_2$/ZGOCB-NH_2 solution (300 μL, 0.5 $mg\cdot mL^{-1}$) on a 7 T MRI system were measured. As shown in Figure 5b, the liver of the mouse can be observed and distinguished from the stomach after 20 min post-injection, suggesting the T_1-weighted MRI shows enhanced signal in the liver site with high spatial resolution. Furthermore, the T_1-weighted MRI of the Dox-Gd_2O_3@$mSiO_2$/ZGOCB-FA (0.15 mg) in the H22 tumor-bearing mice was also performed as shown in the Figure S6, suggesting also the excellent tumor-targeting capacity. The *in vitro* and *in vivo* results indicate that after Gd^{3+} doped within the Gd_2O_3@$mSiO_2$/ZGOCB, this kind of nanoprobes give high MRI sensitivity. Hence, this property combined with optical imaging *in vivo* may reduce the contrast agent dose desirable for biomedical application.

***In vitro* and *in vivo* tumor targeting imaging.** To demonstrate the potential use of Gd_2O_3@$mSiO_2$/ZGOCB-FA as efficient tumor targeting nanoprobe, L02 and HepG2 were selected as modal cells since the L02 and HepG2 have low and strong folate receptor expression, respectively. [16]

The results *in vitro* indicated the Gd_2O_3@$mSiO_2$/ZGOCB-FA possessed better ability to target HepG2 tumor cells than the normal L02 cells (**Figure 6**a, afterglow signal of the HepG2 cells was much stronger than that of L02 cells). As time goes on, the signal from the HepG2 cells was higher enough to be measured within 40 min while the L02 case was weak. The interactions between the cells and Gd_2O_3@$mSiO_2$/ZGOCB-FA were also investigated using confocal microscopy (Figure 6b). Owing to the overexpressed FA receptor on the tumor cell surface, the intracellular uptake of Gd_2O_3@$mSiO_2$/ZGOCB-FA for the HepG2 cells was much higher than that for L02 cells, indicating the Gd_2O_3@$mSiO_2$/ZGOCB-FA has excellent *in vitro* tumor-targeting capacity. For detecting with high sensitivity, the detection accuracy is a key factor. Namely, it is also needed to determine the correlation between the signal and tumor cell numbers for making clear the minimum degree of detection. The signal strength was decreasing with the HepG2 cell number decreasing and the signal was still detectable till the cell number to 196 (SNR = 5, Figure S7). A good correlation between signal and cell number can be obtained, suggesting Gd_2O_3@$mSiO_2$/ZGOCB-FA can be employed to detect cancer cells with high SNR.

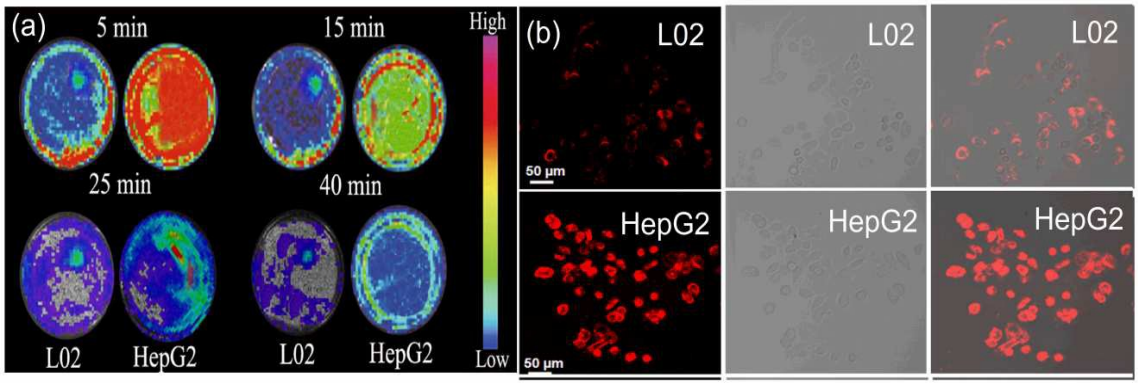

Figure 6. (a) Luminescence images of L02 and HepG2 cells incubated with Gd_2O_3@$mSiO_2$/ZGOCB-FA for 2 h. (b) Confocal microscopic images of HepG2 and L02 cells treated with Gd_2O_3@$mSiO_2$/ZGOCB-FA for 2 h, (left) luminescence images, (middle) white light images, and (right) white light images overlaid on top luminescence images.

. To investigate the potential of Gd_2O_3@$mSiO_2$/ZGOCB for tumor imaging *in vivo*, after the nanoprobe under UV excitation for 2 min, different numbers of HepG2 cells labeled with the

nanoprobe were immediately injected into the abdomen of a mouse. Obviously, the signal can be captured in the abdomen of the mouse with good correlations (**Figure 7**a), indicating the potential utility of Gd_2O_3@mSiO_2/ZGOCB-FA for tumor cell detection *in vivo*. Even 30 min later, the correlation was still maintained, suggesting Gd_2O_3@mSiO_2/ZGOCB-FA can be employed to realize precise tumor targeting detection for a long time. Most of the current long persistent phosphors can only be excited effectively under blue or/and UV light which can hardly penetrate the deep tissue of animals. [6d, 14a, 17] The PLE band located at 600-650 nm (Figures 4b and S5a) is in the transmission window of biological tissue and thus gives the opportunity to recharge the energy-exhausted Gd_2O_3@mSiO_2/ZGOCB-FA in deep tissue *in situ*. Therefore, *in vivo* and *in situ* repeatable excitation can be expected. Figure 7b showed the real-time and high SNR imaging using a red LED lamp (600-700 nm) for 2 min stimulation after 3 h of emission decay. The signal could be recovered and detected at the tumor cells site. The correlation between the signal and the cell numbers was still in line. The results reveal that the Gd_2O_3@mSiO_2/ZGOCB not only can be used as real-time and high SNR nanoprobe but also realized continuous *in vivo* and *in situ* tumor-targeting monitoring.

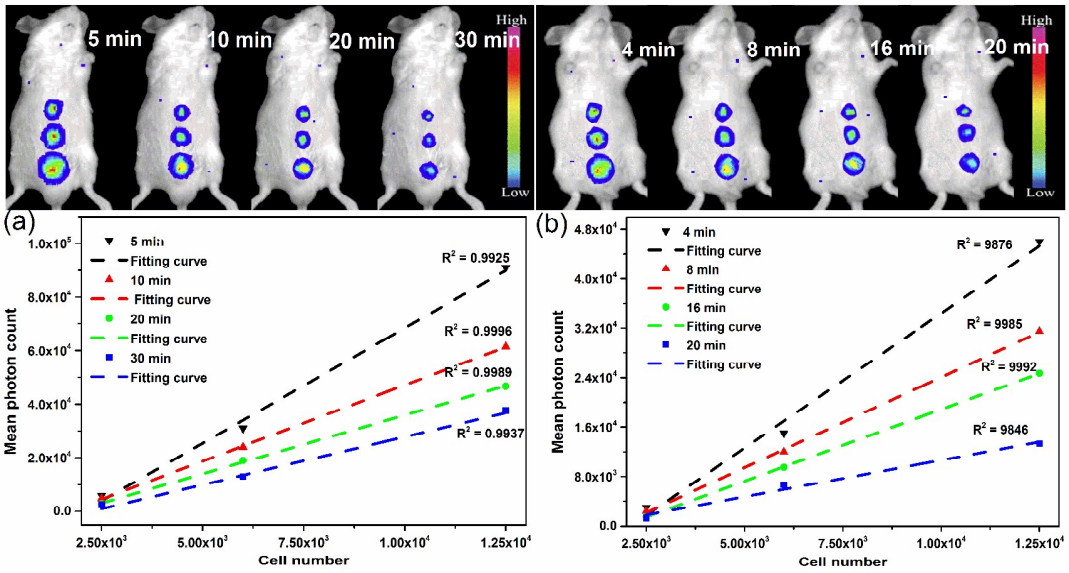

Figure 7. (a) Top, luminescence images *in vivo* after subcutaneous injection of HepG2 cells treated with Gd_2O_3@mSiO_2/ZGOCB-FA (2 min of irradiation with UV lamp before injection). Bottom, correlation between *in vivo* signal and cell number. (b) Top, *in vivo* luminescence images of secondary excitation with a red LED lamp for 2 min, the images were obtained 3 h after subcutaneous injection. Bottom, correlation between *in vivo* signal and cell number.

***In vitro* drug loading and release.** For demonstrating the potential use of Gd_2O_3@$mSiO_2$/ZGOCB as efficient carriers, the commonly used chemotherapeutic drug Dox for cancer therapy was chose as modal drug to evaluate the entrapment efficiency and measure its ability to release the drug. The strong negative charge makes the Gd_2O_3@$mSiO_2$/ZGOCB-FA likely to interact with positively charged Dox *via* classical electrostatic interactions to form Dox-Gd_2O_3@$mSiO_2$/ZGOCB-FA. Compared to the Gd_2O_3@$mSiO_2$/ZGOCB-FA, the BET surface area decreased to 186 $m^2 \cdot g^{-1}$ after loading Dox and the pore volume decreased to 0.1328 $cm^3 \cdot g^{-1}$ (Figure S8a). The decrease of BET surface area and pore volume suggests the mesoporous channels have been further partially filled with Dox. The loading content, defined as the weight of Dox in Gd_2O_3@$mSiO_2$/ZGOCB-FA in relation to the weight of Dox-Gd_2O_3@$mSiO_2$/ZGOCB-FA, was determined to be 7.8%. Meanwhile, the entrapment of Dox was assessed by exploiting strong absorption of Dox at 480 nm (Figure S8b).

Previous studies have reported that drug cells adsorbed into the porous materials were released *via* the Fickian diffusion mechanism. [18] According to this method, *in vitro* cumulative drug release profile was shown in **Figure 8**a for the Dox-Gd_2O_3@$mSiO_2$/ZGOCB-FA under the normal physiological environment (PBS, pH = 7.4, 37°C). The burst release occurs in the starting 50 h followed by a sustained release. The drug release process is overall slow and ~ 99% Dox is released after 65 h. The drug release profile suggests the Gd_2O_3@$mSiO_2$/ZGOCB has potential application in the development of controlled or delayed drug delivery system. Nevertheless, the UV-vis spectra of pure Dox and release Dox were given in Figure 8b, demonstrating the absorption wavelength has no changed. Thus, it can be inferred that Dox was released by its original form. These results suggest the Gd_2O_3@$mSiO_2$/ZGOCB can be adopted as efficiency drug storage/release carriers.

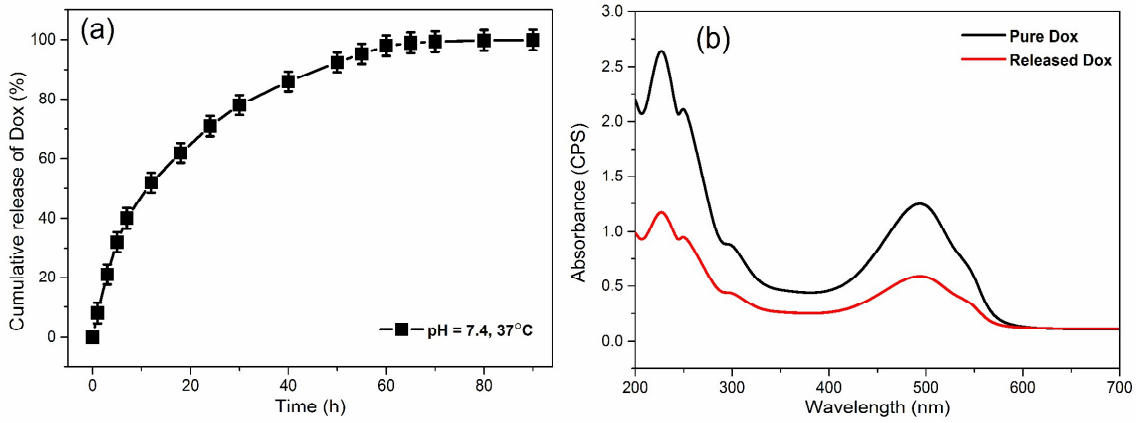

Figure 8. (a) Drug release profile of Dox-Gd_2O_3@$mSiO_2$/ZGOCB-FA. (b) UV-vis spectrum of Dox.

***In vivo* tumor targeting and drug tracking.** To determine the potential application of the Gd_2O_3@$mSiO_2$/ZGOCB as potential trackable drug carriers for tumor targeting and real-time monitoring, the Dox-Gd_2O_3@$mSiO_2$/ZGOCB-FA (0.3 mg) was injected into (*via* tail vein) normal and H22 tumor bearing mice, respectively. [19] The long-lasting luminescence images, acquired after the systemic administration, clearly demonstrate the optical potential of such technology in living animals. Note that the recourse to persistent luminescence allows complete avoidance of autofluorescence from biological tissues and highly sensitive detection *via* living tissues. From chronological observation (**Figure 9**a), the signal from the Dox-Gd_2O_3@$mSiO_2$/ZGOCB-FA in the H22 tumor-bearing mice can be clearly observed in the whole body within the first 10 min and signal at the tumor site can be detected in the entire process (~ 30 min), suggesting the excellent tumor-targeting capacity. The SNR still has a high value (5.4, Figure S9) in the tumor site even after 30 min injection. For comparison, the similar process was also performed on the normal mice and there is almost no signal can be detected at the same site (Figure 9b).

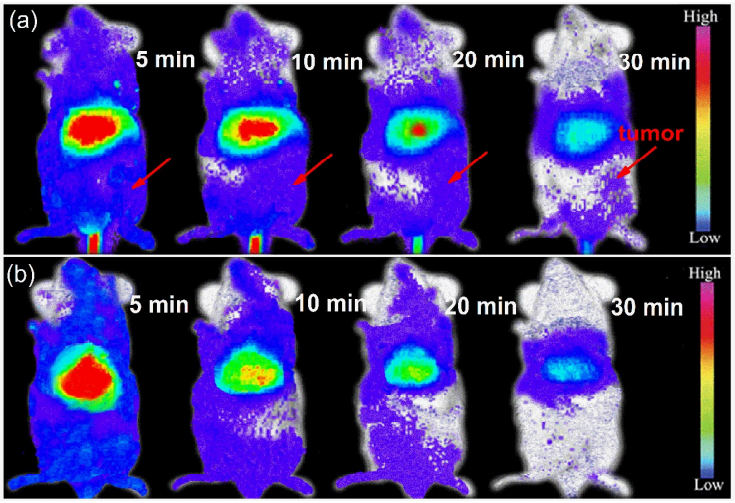

Figure 9. *In vivo* luminescence images of H22 tumor bearing mice (a) and normal mice (b) after intravenous injection of Dox-Gd_2O_3@$mSiO_2$/ZGOCB-FA.

Although long persistent afterglow can be detected *in vivo* due to the excellent optical properties of ZGOCB, the decreasing of intensity over time is unavoidable, which leads to decrease signal and accompany with low detection sensitivity. To enhance the resolution of the tumor image after a relatively long time (i.e., after 3 h), the Dox-Gd_2O_3@$mSiO_2$/ZGOCB-FA was re-excited using a red LED lamp for 2 min. The obvious signal at the tumor site recovered (Figure S10). Meanwhile, due to the blood circulation, more Dox-Gd_2O_3@$mSiO_2$/ZGOCB-FA nanoparticles were accumulated at the tumor site over time and led the tumor site signal exhibited a relatively higher SNR. These results suggest Dox-Gd_2O_3@$mSiO_2$/ZGOCB-FA possessed excellent capacity for repetitive, real-time and high sensitivity imaging *in vivo*.

Finally, the biodistribution of the nanoprobe was investigated by *ex vivo* analysis 6 h after the injection, demonstrating their long term circulation. For *ex vivo* quantification, a UV source was shined on the different organs for 2 min in order to reactivate the persistent luminescence. The Dox-Gd_2O_3@$mSiO_2$/ZGOCB-FA was retained in various organs, including heart, lungs, liver, spleen, kidneys and tumor. Almost no signal can be detected in the heart and kidney while strong signal was observed in the liver and spleen with relatively weak signal originated from the lung and tumor (**Figure 10**). These *ex vivo* imaging results were consistent with the results for tumor imaging *in vivo*.

The long term circulation and widespread organ distribution of the nanoprobe offer a variety of potential imaging targets such as those for cancer or cardiovascular diseases.

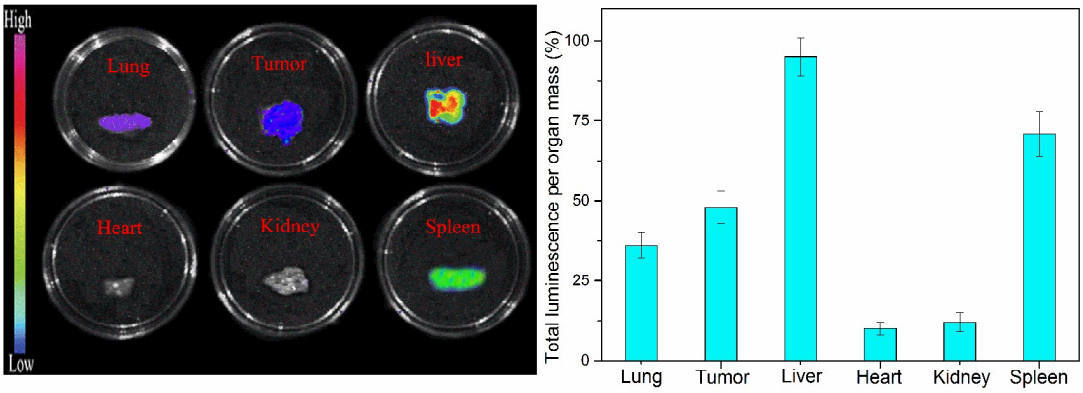

Figure 10. *Ex vivo* image of liver, spleen, kidneys, heart, lung and tumor corresponding biodistrubition for each organ 6 h after systemic injection.

3. Conclusion

The rechargeable red persistent luminescence nanoprobe Gd_2O_3@$mSiO_2$/$ZnGa_2O_4$:Cr^{3+}, Bi^{3+} was designed and synthesized using mesopores core/shell architecture $mSiO_2$ as the reaction templates and carriers. The codoping of Cr^{3+}/Bi^{3+} with slight Zn deficiency significantly improves the persistent luminescence property of the $Zn_{0.97}Ga_2O_{3.97}$: 0.01Cr, 0.02Bi NPs due to suppression of the self-reduction effect of Cr^{3+}. The novel combination with the gadolinium complex not only preserves the excellent red persistent luminescence but also has the paramagnetic property with high longitudinal relaxivity, which endows the Gd_2O_3@$mSiO_2$/$ZnGa_2O_4$:Cr^{3+}, Bi^{3+} possess the multimodal functions including as drug delivery vehicle, optical imaging probe and T_1-weighted MRI contrast agent. The drug loading/release, magnetic and long afterglow luminescent properties of the multifunctional nanoprobe Gd_2O_3@$mSiO_2$/$ZnGa_2O_4$:Cr^{3+}, Bi^{3+} highlights the versatility of nanotechnology and gives access to a large field of biophotonics associated with diagnostics and therapeutics.

4. Experimental Section

Synthesis of persistent luminescence nanoparticles. A biphasic hydrothermal approach was adopted for synthesis of $Zn_{0.97}G_{2-x-y}O_{3.97}$: *x*Cr, *y*Bi NPs with controlled size *via* the hydrolysis of corresponding inorganic salts in a water-toluene system. [20] The synthetic procedure is shown:

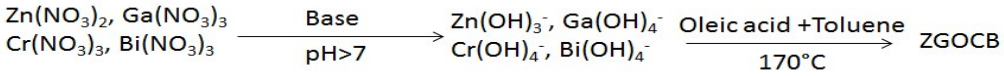

Typically, for obtaining the $Zn_{0.97}G_{1.97}O_{3.97}$: 0.01Cr, 0.02Bi, 1 mmol of $Zn(NO_3)_2$, 2.062 mmol of $Ga(NO_3)_3$, 0.02 mmol of $Cr(NO_3)_3$ and 0.04 mmol of $Bi(NO_3)_3$ were dissolved in 15 ml of deionized water, followed by the addition of tert-butylamine to adjust the pH to the required value with stirring for 30 min. Then, the solution was mixed with an organic solution of oleic acid (2 mL) and toluene (20 mL). The resulting mixture was transferred to a 50 mL Teflon-lined stainless steel autoclave and heated at 150°C for 20 h. Next, the system was cooled to RT and the NPs were precipitated out of the synthesis solution on addition of excess ethanol. The purified products were separated by centrifugation.

The Gd_2O_3@mSiO_2 was obtained according to a previous method with slight modification (see supporting information). [5, 6c, 6d] The mesoporous core/shell structured Gd_2O_3 was synthesized using StÒber method (see supporting information). [21] The multifunctional nanoparticles Gd_2O_3@mSiO_2/ZGOCB was obtained by adsorbing the ZGOCB sol into the pores of Gd_2O_3@mSiO_2 (see supporting information).

***In vitro* MRI:** T_1-weighted MRI was performed on 7 T MRI system (BioSpec 70/20 USR, Bruker, USA). The fixed parameters were set: 1.5 mm of the slice thickness, RT, TR/TE = 100.0/8.8 ms. PLNPs were dispersed in agarose gel at various Gd^{3+} concentrations (0, 0.05, 0.25, 0.5, 0.75 and 1 mM). The relaxation time values (T_1) were measured on the same MRI system by the inversion recovery sequence. The r_1 relaxivity values were calculated *via* the curve fitting of $1/T_1$ relaxation time (s^{-1}) versus the Gd^{3+} concentration. *In vivo MRI:* see supporting information.

Surface modification of Gd_2O_3@mSiO_2/ZGOCB: The surface functionalization of the Gd_2O_3@mSiO_2/ZGOCB was performed according to the existing protocol with slight modification (see supporting information). [3c, 4c, 5, 6b, 6c] **Cytotoxicity test:** Cytotoxicity was evaluated by MTT and

cell apoptosis assays (see supporting information). [3c, 4c, 5, 6a, 6c] **Drug storage and release:** Drug storage and release experiments were conducted according to the previous protocol with some modifications (see supporting information). [6a, 6b, 6c, 22] ***In vitro*** **and** ***in vivo*** **luminescence imaging** and **Characterizations:** see supporting information.

Acknowledgements

We gratefully acknowledge the financial support from the Natural Science Foundation of China (Grant No. 51125005), Fundamental Research Funds for the Central Universities (Grant No.2015ZM035), China Postdoctoral Science Foundation (Grant No. 2014M552019) and the Scientific Research Foundation for the Returned Overseas Chinese Scholars (State Education Ministry).

References

[1] (a) R.Weissleder, M. J. Pittet, *Nature* **2008,** *452*, 580. (b) Q. Liu, Y. Sun, T. S. Yang, W. Feng, C. G. Li, F. Y. Li, *J. Am. Chem. Soc.* **2011,** *133*, 17122. (c) L. Zhou, R. Wang, C. Yao, X. M. Li, C. L. Wang, X. Y. Zhang, C. J. Xu, A. J. Zeng, D. Y. Zhao, F. Zhang, *Nat. Commun.* **2015,** *6*, 6938. (d) J. Zhou, Z. Liu, F. Y. Li, *Chem. Soc. Rev.* **2012,** *41*, 1323. (e) S. V. Eliseeva, J. C. G. Bunzli, *Chem. Soc. Rev.* **2010,** 39, 189. (f) P. Li, S. Zhang, N. N. Fan, H. B. Xiao, W. Zhang, W. Zhang, H. Wang, B. Tang, *Chem. Eur. J.* **2014,** *20,* 16488.

[2] (a) Z. Pan, Y. Y. Lu, F. Liu, *Nat. Mater.* **2012,** *11*, 58. (b) F. Liu, W. Yan, Y. J. Chuang, Z. Zhen, J. Xie, Z. Pan, *Sci. Rep.* **2013,** *3*, 1554. (c) Y. Chen, H. R. Chen, J. L. Shi, *Adv. Mater.* **2013,** *25*, 3144. (d) Q. F. Xiao, X. P. Zheng, W. B. Bu, W. Q. Ge, S. J. Zhang, F. Chen, H. Y. Xing, Q. G. Ren, W. P. Fan, K. L. Zhao, Y. Q. Hua, J. L. Shi, *J. Am. Chem. Soc.* **2013,** *135*, 13041. (e) S. K. Singh, *RSC Adv.* **2014**, 4, 58674.

[3] (a) Q. le Masne de Chermont, C. Chanéac, J. Seguin, F. Pellé, S. Maîtrejean, J. P. Jolivet, D. Gourier, M. Bessodes, D. Scherman, *Proc. Natl. Acad. Sci. U.S.A.* **2007,** *104*, 9266. (b) S. A. Hilderbrand, R. Weissleder, *Curr. Opin. Chem. Biol.* **2010,** *14*, 71. (c) A. Abdukayum, J. Chen, Q. Zhao, X. Yan, *J. Am. Chem. Soc.* **2013,** *135*, 14125. (d) D. Chen, Y. Chen, H. Lu, Z. Ji, *Inorg. Chem.* **2014,** *53*, 8638. (e) D. M. Yan, P. A. Ma, Z. Y. Hou, Z. Y. Cheng, C. X. Li, J. Li, *Chem. Soc. Rev.* **2015,** *44*, 1416. (f) N. Li, Y. H. Li, Y. Y. Han, W. Pan, T. T. Zhang, B. Tang, *Anal. Chem.* **2014,** *86,* 3924.

[4] (a) T. Maldiney, A. Lecointre, B. Viana, A. Bessière, M. Bessodes, D. Gourier, C. Richard, D. Scherman, *J. Am. Chem. Soc.* **2011,** *133*, 11815. (b) Z. J. Li, J. P. Shi, H. W. Zhang, M. Sun, *Opt. Express* **2014,** *22*, 10509. (c) J. L. Li, J. P. Shi, J. S. Shen, H. Z. Man, M. X. Wang, H. W. Zhang, *Nano-Micro Lett.* **2014,** *7*, 138.

[5] T. Maldiney, A. Bessière, J. Seguin, E. Teston, S. K. Sharma, B. Viana, A. J. J. Bos, P. Dorenbos, M. Bessodes, D. Gourier, D. Scherman, C. Richard, *Nat. Mater.* **2014,** *13*, 418.

[6] (a) T. Maldiney, B. Ballet, M. Bessodes, D. Scherman, C. Richard, *Nanoscale* **2014,** *6*, 13970. (b) J. P. Shi, X. Sun, J. L. Li, H. Z. Man, J. S. Shen, Y. K. Yu, H. W. Zhang, *Biomaterials* **2015,** *37*,

260. (c) J. P. Shi, H. X. Fu, X. Sun, J. S. Shen, H. W. Zhang, *J. Mater. Chem. B* **2015,** *3*, 635. (d) Z. Li, Y. Zhang, X. Wu, X. Wu, R. Maudgal, H. Zhang, G. Han, *Adv. Sci.* **2015,** *2*, 1500001.

[7] A. Abdukayum, C. X. Yang, Q. Zhao, J. T. Chen, L. X. Dong, X. P. Yan, *Anal. Chem.* **2014,** *86*, 4096.

[8] A. Bessiere, S. Jacquart, K. Priolkar, A. Lecointre, B. Viana, D. Gourier, *Opt. Express* **2011,** *19*, 10131.

[9] Z. Li, Y. Zhang, X. Wu, L. Huang, D. Li, W. Fan, G. Han, *J. Am. Chem. Soc.* **2015,** *137*, 5304.

[10] (a) C. Kemball, G. D. L. Schreiner, *J. Am. Chem. Soc.* **1950,** *72*, 5605. (b) L. D. Gelb, K. E. Gubbins, *Langmuir* **1998,** *14*, 2097.

[11] R. Mallik, C. Wa, D. S. Hage, *Anal. Chem.* **2007,** *79*, 1411.

[12] (a) B. Viana, A. M. Lejus, D. Vivien, V. Ponçon, G. *J.* Boulon, *Solid State Chem.* **1987,** *71*, 77. (b) I. J. Moraes, R. R. de Souza, O. R. do Nascimento, M. C. Terrile, G. E. Barberis, *Solid State Commun.* **1995,** *95*, 251. (c) R. D. Shannon, *Acta Crystallogr.* **1976,** *A32*, 751. (d) Z. Yi, U. Jumpei, T. Setsuhisa, *Appl. Phys. Express* **2013,** *6*, 052602.

[13] Y. Zhuang, J. Ueda, S. Tanabe, *Opt. Mater. Express* **2012,** *2*, 1378.

[14] (a) F. Clabau, X. Rocquefelte, S. Jobic, P. Deniard, M. H. Whangbo, A. Garcia, T. Le Mercier, *Chem. Mater.* **2005,** *17*, 3904. (b) Z. Ji, S. Tian, W. Chen, Z. Kong, J. Wu, *Radiat. Meas.* **2013,** *59*, 210.

[15] H. Freiser, Q. Fernando, *Ionic Equilibria in Analytical Chemsitry*. Wiley: New York, 1997; p. 110-113.

[16] (a) Y. Xu, X. Jin, Q. Ping, J. Cheng, M. Sun, F. Cao, W. You, D. Yuan, *J. Control. Release* **2010,** *146*, 299. (b) J. Sudimack, R. J. Lee, *Adv. Drug Deliver. Rev.* **2000,** *41*, 147.

[17] (a) L. C. V. Rodrigues, J. Holsa, M. Lastusaari, M. C. F. C. Felinto, H. F. Brito, *J. Mater. Chem. C* **2014,** *2*, 1612. (b) L. C. V. Rodrigues, H. F. Brito, J. Hölsä, R. Stefani, M. C. F. C. Felinto, M. Lastusaari, T. Laamanen, L. A. O. Nunes, *J. Phys. Chem. C* **2012,** *116*, 11232.

[18] W. Zhao, H. Chen, Y. Li, L. Li, M. Lang, J. Shi, *Adv. Funct. Mater.* **2008,** *18*, 2780.

[19] (a) J. Geng, K. Li, D. Ding, X. Zhang, W. Qin, J. Liu, B. Z. Tang, B. Liu, *Small* **2012,** *8*, 3655. (b) K. Li, D. Ding, D. Huo, K. Y. Pu, N. N. P. Thao, Y. Hu, Z. Li, B. Liu, *Adv. Funct. Mater.* **2012,** *22*, 3107.

[20] (a) M. Brust, M. Walker, D. Bethell, D. J. Schiffrin, R. Whyman, *Chem. Soc., Chem. Commun.* **1994,** *7*, 801. (b) Y. Xia, Y. Xiong, B. Lim, S. E. Skrabalak, *Angew. Chem. Int. Edit.* **2009,** *48*, 60.

[21] H. Rutledge, B. L. Oliva-Chatelain, S. J. Maguire-Boyle, D. L. Flood, A. R. Barron, *Mat. Sci. Semicon. Proc.* **2014,** *17*, 7.

[22] Y. Dai, P. A. Ma, Z. Cheng, X. Kang, X. Zhang, Z. Hou, C. Li, D. Yang, X. Zhai, J. Lin, *ACS Nano* **2012,** *6*, 3327.

Graphical abstract

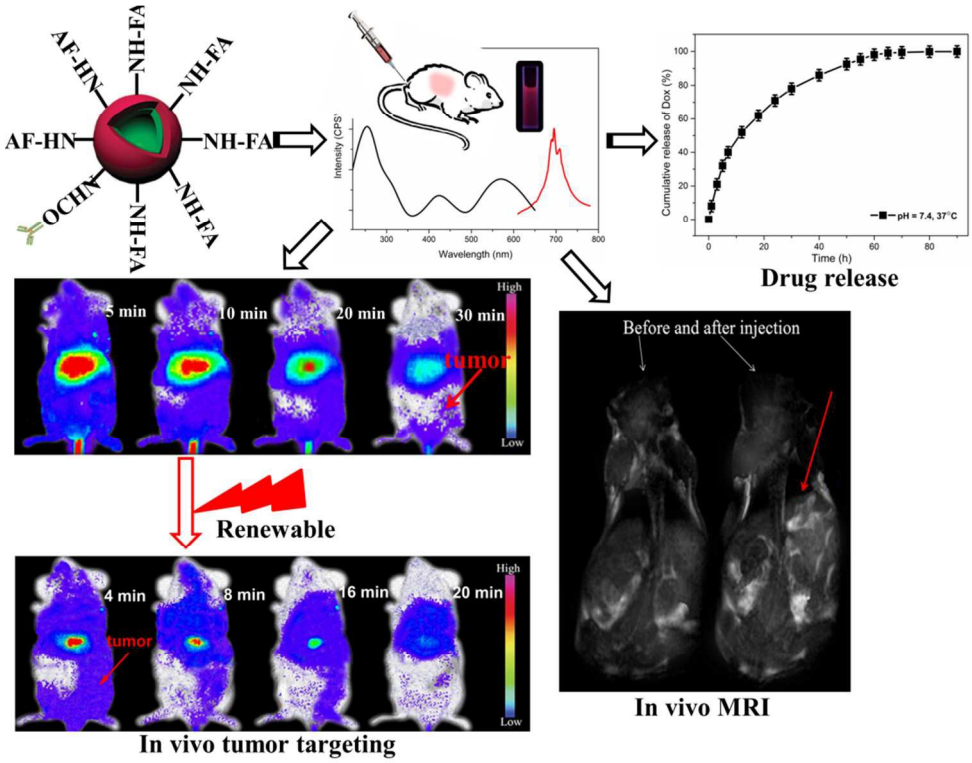

The multifunctional core/shell Gd_2O_3@mSiO_2/ZGOCB nanoparticles, which possess the ability to serve simultaneously as drug delivery vehicles, optical imaging probe and magnetic resonance imaging agents, has been prepared using mSiO_2 as morphology-controlling templates. The drug storage/release, magnetic and long afterglow luminescent properties make the nanoprobe a promising candidate as a potential platform for therapeutics and diagnostics of reactive species in living cells or in vivo with the help of optical imaging and MRI techniques.